A&A 664, A36 (2022)
https://doi.org/10.1051/0004-6361/202142919

Astronomy & Astrophysics

VLBI observations of GRB 201015A, a relatively faint GRB with a hint of very high-energy gamma-ray emission

S. Giarratana[1,2], L. Rhodes[3,4], B. Marcote[5], R. Fender[3,6], G. Ghirlanda[7,8], M. Giroletti[2], L. Nava[7,9,10], J. M. Paredes[11], M. E. Ravasio[7,12,17], M. Ribó[11,13], M. Patel[14], J. Rastinejad[15], G. Schroeder[15], W. Fong[15], B. P. Gompertz[16], A. J. Levan[17,18], and P. O'Brien[14]

[1] Department of Physics and Astronomy, University of Bologna, via Gobetti 93/2, 40129 Bologna, Italy
e-mail: stefano.giarratana2@unibo.it
[2] INAF Istituto di Radioastronomia, via Gobetti 101, 40129 Bologna, Italy
[3] Astrophysics, Department of Physics, University of Oxford, Keble Road, Oxford OX1 3RH, UK
[4] Max-Planck-Institut für Radioastronomie, Auf dem Hügel 69, 53121 Bonn, Germany
[5] Joint Institute for VLBI ERIC, Oude Hoogeveensedijk 4, 7991 PD Dwingeloo, The Netherlands
[6] Department of Astronomy, University of Cape Town, Private Bag X3, Rondebosch 7701, South Africa
[7] INAF Osservatorio Astronomico di Brera, Via E. Bianchi 46, 23807 Merate, Italy
[8] INFN Sezione di Milano-Bicocca, Piazza della Scienza 3, 20126 Milano, Italy
[9] INFN Sezione di Trieste, via Valerio 2, 34149 Trieste, Italy
[10] Institute for Fundamental Physics of the Universe (IFPU), 34151 Trieste, Italy
[11] Departament de Física Quàntica i Astrofísica, Institut de Ciències del Cosmos, Universitat de Barcelona, IEEC-UB, Martí i Franquès 1, E08028 Barcelona, Spain
[12] Università degli Studi di Milano-Bicocca, piazza dell'Ateneo Nuovo 1, 20126 Milano (MI), Italy
[13] Serra Húnter Fellow
[14] School of Physics and Astronomy, University of Leicester, University Road, Leicester, LE1 7RH, UK
[15] Center for Interdisciplinary Exploration and Research in Astrophysics and Department of Physics and Astronomy, Northwestern University, 2145 Sheridan Road, Evanston, IL 60208-3112, USA
[16] School of Physics and Astronomy, University of Birmingham, Birmingham, B15 2TT, UK
[17] Department of Astrophysics/IMAPP, Radboud University, PO Box 9010, 6500 GL, The Netherlands
[18] Department of Physics, University of Warwick, Coventry, CV4 7AL, UK

Received 15 December 2021 / Accepted 24 May 2022

ABSTRACT

Context. A total of four long-duration gamma-ray bursts (GRBs) have been confirmed at very high-energy (≥100 GeV) with high significance, and any possible peculiarities of these bursts will become clearer as the number of detected events increases. Multi-wavelength follow-up campaigns are required to extract information on the physical conditions within the jets that lead to the very high-energy counterpart, hence they are crucial to reveal the properties of this class of bursts.

Aims. GRB 201015A is a long-duration GRB detected using the MAGIC telescopes from ∼40 s after the burst. If confirmed, this would be the fifth and least luminous GRB ever detected at these energies. The goal of this work is to constrain the global and microphysical parameters of its afterglow phase, and to discuss the main properties of this burst in a broader context.

Methods. Since the radio band, together with frequent optical and X-ray observations, proved to be a fundamental tool for overcoming the degeneracy in the afterglow modelling, we performed a radio follow-up of GRB 201015A over 12 different epochs, from 1.4 days (2020 October 17) to 117 days (2021 February 9) post-burst, with the Karl G. Jansky Very Large Array, e-MERLIN, and the European VLBI Network. We include optical and X-ray observations, performed respectively with the Multiple Mirror Telescope and the *Chandra* X-ray Observatory, together with publicly available data, in order to build multi-wavelength light curves and to compare them with the standard fireball model.

Results. We detected a point-like transient, consistent with the position of GRB 201015A until 23 and 47 days post-burst at 1.5 and 5 GHz, respectively. No emission was detected in subsequent radio observations. The source was also detected in optical (1.4 and 2.2 days post-burst) and in X-ray (8.4 and 13.6 days post-burst) observations.

Conclusions. The multi-wavelength afterglow light curves can be explained with the standard model for a GRB seen on-axis, which expands and decelerates into a medium with a homogeneous density. A circumburst medium with a wind-like profile is disfavoured. Notwithstanding the high resolution provided by the VLBI, we could not pinpoint any expansion or centroid displacement of the outflow. If the GRB is seen at the viewing angle θ that maximises the apparent velocity $\beta_{\rm app}$ (i.e. $\theta \sim \beta_{\rm app}^{-1}$), we estimate that the Lorentz factor for the possible proper motion is $\Gamma_\alpha \leq 40$ in right ascension and $\Gamma_\delta \leq 61$ in declination. On the other hand, if the GRB is seen on-axis, the size of the afterglow is ≤5 pc and ≤16 pc at 25 and 47 days. Finally, the early peak in the optical light curve suggests the presence of a reverse shock component before 0.01 days from the burst.

Key words. radio continuum: general – gamma-ray burst: general – gamma-ray burst: individual: GRB 201015A

1. Introduction

Long-duration gamma-ray bursts (GRBs) are extremely powerful flashes that generally last more than 2 s (Mazets et al. 1981; Norris et al. 1984; Kouveliotou et al. 1993) and whose prompt emission is detected mainly in the γ-ray and X-ray domains. They are thought to signpost the catastrophic death of a massive star (see e.g. Galama et al. 1998; Piran 2004, Kumar & Zhang 2015) that has previously expelled its hydrogen envelope into the surrounding medium (Woosley & Heger 2006), and the subsequent formation of a spinning stellar mass black hole (BH; Woosley 1993; Paczyński 1998) or neutron star (NS; Usov 1992). This newborn central engine may power and launch relativistic jets of ejected matter within which internal shocks (Rees & Mészáros 1994) or magnetic reconnections (Drenkhahn & Spruit 2002) can convert a fraction of the bulk kinetic energy into the observed short-lived γ-ray radiation (Mészáros 2002). These expanding jets interact with the circumburst medium (Rees & Mészáros 1992; Mészáros & Rees 1993), triggering both a forward shock and a reverse shock (RS; Mészáros 2002). The electrons at the shock fronts are accelerated to relativistic energies, producing a long-lived afterglow through synchrotron emission, which can be observed from high energies (GeV) through X-rays, optical, and near-infrared down to the radio bands (see e.g. Gehrels et al. 2009; Kouveliotou et al. 2012).

The radio light curve is fundamental for the afterglow modelling; together with frequent optical and X-ray observations, it helps us to better constrain the multi-dimensional parameter space and to distinguish between different scenarios, providing relevant information to understand the progenitor's nature and the GRB origin. Nevertheless, the detection rate of GRBs observed in the radio band is only ∼30%, and an even smaller number of events have multi-epoch observations (Chandra & Frail 2012). In events where radio emission has been detected, it can be observed for months or even years after the burst (Piran 2004). It provides a powerful tool to better constrain not just the internal jet physics, but also the geometry and physical evolution of the jet. Evidence of scintillation has helped study the expansion velocity of the outflow (Frail et al. 1997), achromatic light curve behaviour can inform on jet opening angles ('jet breaks') and constrain the transition from relativistic to non-relativistic expansion (Frail et al. 2004), which can be used to infer the total kinetic energy by performing radio calorimetry (see e.g. Berger et al. 2004; Frail et al. 2005). For the nearest events the high angular resolution provided by Very Long Baseline Interferometry (VLBI) has proved to be complementary to studying the afterglow; it is a unique tool to measure the expansion (Taylor et al. 2004) and the centroid displacement (Mooley et al. 2018) of the outflow, to constrain its size (Ghirlanda et al. 2019), and to distinguish the proper compact afterglow emission from contaminating components within the host galaxy.

At the opposite end of the spectrum, only four GRBs have a bona fide detection in the very high-energy (VHE; ≥100 GeV) range at either early epochs (e.g. GRB 190114C, 300 GeV–1 TeV; MAGIC Collaboration 2019 and GRB 201216C; Blanch et al. 2020b) or at later times deep in the afterglow phase (e.g. GRB 180720B, 100–400 GeV; Abdalla et al. 2019 and GRB 190829A, 180 GeV–3.3 TeV; H.E.S.S. Collaboration 2021). Studying this emission component allows the physical properties of the emitting region and/or of the shocked accelerated particles to be constrained, and the most natural interpretation for this VHE emission is the inverse-Compton scattering of synchrotron photons, known as synchrotron self-Compton (SSC) emission. Based on the very few events detected so far, it seems that the VHE emission characterises both very energetic events, such as GRB 180720B and GRB 190114C, and low-energy events, such as 190829A, but any possible peculiarities of VHE detected bursts will become clearer as the sample of events increases. However, multi-wavelength follow-up of these events has proved a fundamental tool to test the afterglow emission model; for example, for GRB 190829A the VHE emission detected by the H.E.S.S. telescopes was first interpreted as synchrotron emission (H.E.S.S. Collaboration 2021), while multi-wavelength follow-up studies agree on an SSC emission origin (Salafia et al. 2022; Zhang et al. 2021; Fraija et al. 2021).

GRB 201015A was discovered on 2020 October 15 at 22:50:13 UT as a multi-peaked 10 s GRB by the Neil Gehrels *Swift* Burst Alert Telescope (hereafter *Swift*/BAT) (D'Elia et al. 2020). Subsequent observations reported the presence of an associated transient in the optical (Lipunov et al. 2020a,b; Malesani et al. 2020; Ackley et al. 2020; Hu et al. 2020; de Ugarte Postigo et al. 2020; Zhu et al. 2020a,b; Belkin et al. 2020a,b; Jelinek et al. 2020; Grossan et al. 2020; Rastinejad et al. 2020; Kumar et al. 2020a; Moskvitin et al. 2020; Pozanenko et al. 2020), X-rays (Kennea et al. 2020; Fletcher et al. 2020; Gompertz et al. 2020; D'Elia & Swift Team 2020), UV (Marshall et al. 2020), and radio (Fong et al. 2020) bands. Remarkably, GRB 201015A was observed by the Major Atmospheric Gamma-ray Imaging Cherenkov (MAGIC) telescopes about 40 s after the *Swift* trigger, and a hint of a VHE counterpart with a significance $\geq 3.5\sigma$ was reported from preliminary analyses (Blanch et al. 2020a; Suda et al. 2021). With the *Fermi* Gamma-ray Burst Monitor (GBM) spectrum, Minaev & Pozanenko (2020) suggested that this burst is consistent with the $E_{\rm peak} - E_{\rm iso}$ Amati relation (Amati et al. 2002) for long-duration GRBs, with an isotropic equivalent energy of $E_{\rm iso} \simeq (1.1 \pm 0.2) \times 10^{50}$ erg. If confirmed, this would be the fifth and least luminous GRB ever detected in this band.

Optical spectroscopy in the 3700–7800 Å range revealed a redshift for the source of ∼0.426 (de Ugarte Postigo et al. 2020; Izzo et al. 2020). To date, all the GRBs that have been detected at VHE have relatively low redshifts: 0.654, 0.425, 0.0785, and 1.1 for GRB 180720B, GRB 190114C, GRB 190829A, and GRB 201216C, respectively (Vreeswijk et al. 2018; Selsing et al. 2019; Valeev et al. 2019; Vielfaure et al. 2020); their isotropic equivalent energies span three orders of magnitude (Rhodes et al. 2020a).

In this paper, we present a multi-wavelength follow-up campaign of GRB 201015A performed with the Karl G. Jansky Very Large Array (VLA), the enhanced Multi Element Remotely Linked Interferometer Network (e-MERLIN), the European VLBI Network (EVN), the Multiple Mirror Telescope (MMT), and the *Chandra* X-ray Observatory (*Chandra*). The observations are presented in Sect. 2, while the results are shown in Sect. 3. We exploit the standard model for GRB afterglows in Sect. 4 to explain the multi-wavelength observations, and we compare our results for GRB 201015A with previous GRBs in Sect. 5. We conclude with a brief summary in Sect. 6. Throughout the paper we assume a standard Λ-CDM cosmology with $H_0 = 69.32\,{\rm km\,Mpc^{-1}\,s^{-1}}$, $\Omega_{\rm m} = 0.286$, and $\Omega_\Lambda = 0.714$ (Hinshaw et al. 2013). With this cosmology, 1″ corresponds to roughly 5.6 kpc at $z = 0.426$.

2. Observations

2.1. VLA observations at 6 GHz

Observations with the VLA were performed 1.41 days post-burst (PI: Fong; project code: 19B-217) at a central frequency of 5.7 GHz with a bandwidth of 1.6 GHz (*C* band). The target and the phase calibrator J2355+4950 were observed in eight-minute cycles, with seven minutes on the former and one minute on the latter. The distance between the target and the phase calibrator is about 4.5°. Finally, 3C147 was used as bandpass and flux calibrator. The data were calibrated using the CASA pipeline, and they were subsequently imaged with the `tclean` task in CASA (Version 5.1.1., McMullin et al. 2007).

2.2. e-MERLIN observations at 1.5 GHz

We started observing at 1.5 GHz with e-MERLIN 20 days post-burst (2020 November 4; PI: Rhodes, project code: DD10003) with two further observations 23 (2020 November 7) and 101 (2021 January 24) days post-burst. The observations were made at a central frequency of 1.51 GHz with a bandwidth of 512 MHz (*L* band). For each epoch the target and phase calibrator, J2353+5518, were observed in ten-minute cycles, with seven minutes on the former and three on the latter. The distance between the phase calibrator and the target is about 3°. Each observation ended with scans of the flux (J1331+3030) and bandpass calibrators (1407+2827). The data were reduced using the custom e-MERLIN pipeline[1]. The calibrated measurement sets were imaged in CASA (Version 4.7).

2.3. e-MERLIN observations at 5 GHz

Observations at 5 GHz with e-MERLIN were performed 21 (2020 November 5), 24 (November 8), 60 (December 14), 85 (2021 January 8), and 100 (January 23) days post-burst (PI: Giroletti; project code: DD10004). All epochs but December 14 were centred at 4.50–5.01 GHz (*C* band) with a bandwidth of 512 MHz divided into four spectral windows of 128 MHz each. For December 14, the frequency range was within 6.55–7.06 GHz (*C* band). The data were first pre-processed with the CASA e-MERLIN pipeline using J1407+2827 as bandpass calibrator and J1331+3030 as flux calibrator. Two phase calibrators were used: J2353+5518, a fainter one on a rapid cycle, and J2322+5057, a brighter one used less frequently (once per hour) to correct for both short- and long-term atmospheric effects. All epochs were observed in eight-minute cycles, with six minutes on the target and two minutes on J2353+5518.

On November 5, an electronic problem occurred and the Defford antenna missed the bandpass and flux calibrators; consequently, the pipeline automatically flagged out this antenna, and there was a considerable data loss. To recover it we performed a further calibration of this epoch. We built a model for J0319+4130 using the pipeline results first, and we subsequently calibrated the data manually using the J0319+4130 model as bandpass and flux calibrator, improving the final image output. After the calibration, we cleaned the dirty image with the `tclean` task in CASA (Version 5.1.1.).

On November 8, the Knockin antenna lost one polarisation channel, and an improved image was achieved using only J2322+5057 for the phase calibration, which is about 3.3° from the target source.

[1] https://github.com/e-merlin/eMERLIN_CASA_pipeline

2.4. EVN observations at 5 GHz

Observations at 5 GHz with EVN were performed 25 (2020 November 9), 47 (December 1), and 117 (2021 February 9) days post-burst (PI: Marcote; project code: RM016). The first epoch (2020 November 9) was conducted at a maximum bitrate of 4 Gbps per station, dividing the full band upon correlation into 16 spectral windows of 32 MHz and 64 frequency channels each, covering the frequency range of 4.57–5.11 GHz (*C* band). The other two following epochs were conducted at a lower rate of 2 Gbps, resulting in eight spectral windows of 32 MHz and 64 frequency channels each, covering the frequency range of 4.77–5.05 GHz. All observations were correlated in real time (e-EVN operational mode) at JIVE (the Netherlands) using the SFXC software correlator (Keimpema et al. 2015).

The following sources were used as fringe finders and/or bandpass calibrators among the different epochs: BL LAC, J0854+2006, 3C 84, J0555+3948, and J0102+5824. The same phase calibrator as in the e-MERLIN observations was used: J2353+5518, in a phase-referencing cycle of 4.5 min on the target source and 1.5 min on the phase calibrator. The source J2347+5142 was observed as a check source to account for possible phase-referencing losses.

The EVN data were reduced using `AIPS`[2] (Greisen 2003) and `Difmap` (Shepherd et al. 1994) following standard procedures. An a priori amplitude calibration method was performed using the known gain curves and system temperature measurements recorded individually on each station during the observation. We manually flagged data affected by radio frequency interference (RFI) and then we fringe-fitted and bandpass-calibrated the data using the fringe finders and the phase calibrator. We imaged and self-calibrated the phase calibrator in `Difmap` to improve the final calibration of the data. We used the same model of the phase calibrator, obtained from the 2020 December 1 epoch, to improve the calibration of all epochs. We note that we chose this epoch because it produced the most reliable image of J2353+5518 in terms of amplitude scales at all baseline lengths (including the short spacing given by the e-MERLIN stations). No apparent changes in the calibrator were observed among these three observations. The obtained solutions were then transferred to the target scans, which were subsequently imaged for each epoch. The check source J2347+5142 was also imaged and self-calibrated, confirming that no significant losses ($\lesssim$10–20%) were present in the obtained amplitudes due to the phase-referencing technique. We note that the Shanghai 65 m Radio Telescope (Tianma) and the Nanshan 25 m Radio Telescope (Urumqi) only participated in the first observation, and since they provided the longest baselines the resolution for the other two epochs decreases significantly (see Table 1).

2.5. Optical observations and public data

At 1.4, 2.2, and 4.3 days post-burst, we observed the position of the afterglow in the *i* and *z* bands with the Binospec instrument mounted on the 6.5 m MMT (PI: Fong; project code: 2020c-UAO-G204-20B). We reduced our images using a custom Python pipeline[3] and registered the images to the USNO-B1 catalogue (Monet et al. 2003) using standard IRAF tasks

[2] The Astronomical Image Processing System (`AIPS`) is a software package produced and maintained by the National Radio Astronomy Observatory (NRAO).

[3] https://github.com/CIERA-Transients/Imaging_pipelines/

Table 1. Radio observations performed with the VLA, e-MERLIN, and EVN in the *L* and *C* bands.

Date	UTC (hh:mm)	T–T_0 (days)	T_s (h)	ν (GHz)	Peak brightness (μJy beam^{-1})	r.m.s. [μJy/beam^{-1}]	Array	Beam size
2020/10/17	8:58–9:38	1.4	0.7	4.23–7.10	132	5	VLA	1.70″× 1.14″
2020/11/04	21:25–06:30	20	9.2	1.25–1.76	213	34	e-MERLIN	0.18″× 0.12″
2020/11/05	20:35–14:00	21	6.1	4.50–5.01	107	17	e-MERLIN	0.06″× 0.04″
2020/11/07	22:00–11:40	23	14	1.25–1.76	261	40	e-MERLIN	0.19″× 0.12″
2020/11/08	23:30–08:30	24	3.9	4.50–5.01	116	26	e-MERLIN	0.06″× 0.04″
2020/11/09	13:00–23:00	25	4.2	4.57–5.11	85	9	EVN	1.8 mas × 0.9 mas
2020/12/01	13:00–23:00	47	4.4	4.77–5.05	73	10	EVN	3.4 mas × 2.8 mas
2020/12/14	09:18–12:43	60	1.4	6.55–7.06	–	43	e-MERLIN	0.12″× 0.07″
2021/01/08	12:34–03:10	85	6.9	4.50–5.01	–	19	e-MERLIN	0.04″× 0.04″
2021/01/23	17:35–08:55	100	8.9	4.50–5.01	–	16	e-MERLIN	0.07″× 0.03″
2021/01/24	11:00–01:20	101	14	1.25–1.76	–	57	e-MERLIN	0.17″× 0.14″
2021/02/09	13:00–18:00 & 06:00–11:00	117	5.0	4.77–5.05	–	13	EVN	3.1 mas × 3.6 mas

Notes. T–T_0 is the total time from the GRB trigger to half of the observation, while T_s is the total time on source. The 1σ r.m.s. noise shown does not include the systematic flux density uncertainty (which we consider as 5% for the VLA and 10% for e-MERLIN and EVN throughout the work).

(Tody 1993). In the first two epochs we clearly detected an uncatalogued source in both bands that did not appear in our deep image at 4.3 days post-burst. To remove any contamination from the nearby galaxy, we performed image subtractions between the first two epochs and the final epoch using `HOTPANTS` (Becker 2015). We then calibrated the images to the PanSTARRS Data Release 2 catalogue (Chambers et al. 2016) and performed aperture photometry on the image subtractions with the IRAF/`phot` task.

We gathered additional optical information from the public GCN Circulars Archive, and the detected emission was deabsorbed with the `dust_extinction` Python package[4], using a Galactic extinction $A_v = 0.93$ (Schlafly & Finkbeiner 2011).

2.6. X-ray observations and public data

We obtained the *Swift* X-ray Telescope (XRT) unabsorbed flux light curve integrated in the 0.3–10 keV energy range from the Swift Burst Analyzer[5] provided by the UK *Swift* Science Data Centre at the University of Leicester (UKSSDC, Evans et al. 2007, 2009).

Moreover, we obtained two epochs of *Chandra* observations with the Advanced CCD Imaging Spectrometer (ACIS) in very faint mode (PI: Gompertz; project code: 22400511). Exposures were centred around 8.4 and 13.6 days after trigger, with exposure times of 30 ks and 45 ks, respectively. The data were analysed using CIAO v4.14 and XSPEC v12.11.1, following the *Chandra* X-ray Observatory science threads[6].

3. Results

3.1. Radio

A point-like source was clearly visible with the VLA 1.4 days post-burst with a peak brightness of 132 ± 8 μJy beam^{-1}, where the uncertainty includes the r.m.s. noise and a 5% calibration error added in quadrature. The r.m.s. noise uncertainty is 5 μJy beam^{-1}, and therefore the detection has a significance of 26σ confidence. The source was found at a position (J2000) $\alpha = 23^h37^m16.403^s$, $\delta = 53°24'56.39''$, with an uncertainty of 0.14″ (1/10 of the beam size, Taylor et al. 1999). Thanks to the wide bandwidth and high signal-to-noise ratio, we were able to split the data in four spectral windows in order to estimate the spectral index β, where the flux density is $F \propto \nu^\beta$. We found $\beta \simeq 2.5$. To further improve this estimate, we produced a spectral map with the `tclean` task in CASA by setting nterms = 2 and deconvolver = 'mtmfs'. We found $\beta = 2.3 \pm 0.1$ at the peak of the target emission. We attribute the emission to the afterglow of GRB 201015A. Finally, we divided the one-hour observation into two intervals of equal duration and determined the peak brightness in each one, which turned out to be 126 ± 9 μJy beam^{-1} and 144 ± 10 μJy beam^{-1} (see Fig. 2, blue stars).

The resulting images from the first and second e-MERLIN epoch at 1.5 GHz showed a point source with a peak brightness of 213 ± 40 μJy beam^{-1} and 261 ± 48 μJy beam^{-1}, where the quoted uncertainty includes the r.m.s. noise and a 10% calibration error added in quadrature, at the position (J2000) $\alpha = 23^h37^m16.423^s$, $\delta = +53°24'56.43''$. The r.m.s. noise uncertainties are 34 μJy beam^{-1} and 40 μJy beam^{-1}, hence the detections have a significance of 6.2 and 6.5σ confidence, respectively. The uncertainty on the position, which was computed as the ratio between the beam size and the signal-to-noise ratio (Taylor et al. 1999), is 0.03″. Unfortunately, the observation at 101 days was heavily affected by RFI and as a result we obtained a 5σ upper limit of 285 μJy beam^{-1}. The data are shown in Fig. 2 as gold squares.

At 5 GHz a point-like transient was clearly detected with e-MERLIN on November 5 (Fig. 1) at the position (J2000) of $\alpha = 23^h37^m16.422^s$, $\delta = 53°24'56.44''$. The uncertainty on the position is 0.01″. The point-like source was also detected on November 8 at the position (J2000) $\alpha = 23^h37^m16.419^s$, $\delta = 53°24'56.33''$. The uncertainty on the position is 0.02″. Although both positions are in agreement with the coordinates provided by the VLA, we note that they are not consistent with each other at 3σ confidence level. We ascribe the offset in the position to the phase calibration of the second epoch: if the phase calibrator is observed less frequently (i.e. once per hour), it may not be able to trace perfectly the short-term atmospheric effects, and therefore correct for them. Nevertheless, we were not able to improve the phase calibration further. The measured peak brightness is 107 ± 20 μJy beam^{-1} and 116 ± 28 μJy beam^{-1}

[4] https://dust-extinction.readthedocs.io/en/stable/
[5] https://www.swift.ac.uk/burst_analyser/01000452/
[6] https://cxc.harvard.edu/ciao/

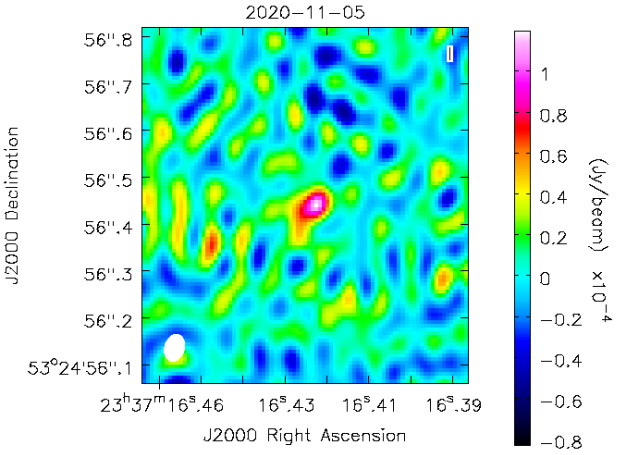

Fig. 1. e-MERLIN detection on 2020 November 5. The synthesised beam is shown in the lower left corner.

for November 5 and 8, respectively, where the quoted uncertainty includes the r.m.s. noise uncertainty and a 10% calibration error added in quadrature. The r.m.s. noise uncertainties are 17 μJy beam^{-1} and 26 μJy beam^{-1}, hence the detections have a significance of 6.3 and 4.5σ confidence, respectively. On December 14, January 8, and January 23 no source was detected; the r.m.s. noise is 43, 19, and 16 μJy beam^{-1}, respectively. The data are shown in Fig. 2 as blue dots.

GRB 201015A was detected as a point-like source also in the first two epochs with EVN at 5 GHz (25 and 47 days after the burst) at a consistent (J2000) position of $\alpha = 23^{\rm h}37^{\rm m}16.42232^{\rm s} \pm 0.2$ mas, $\delta = 53°24'56.4392'' \pm 0.3$ mas. The quoted uncertainties include the statistical uncertainties (0.05 and 0.12 mas for α and δ, respectively), the uncertainties in the absolute International Celestial Reference Frame position of the phase calibrator (0.11 mas), and check source (0.15 mas; Beasley et al. 2002; Gordon et al. 2016), and the estimated uncertainties from the phase-referencing technique (0.13 and 0.2 mas; Pradel, et al. 2006) added in quadrature.

The derived peak brightness measurements are 85 ± 13 μJy beam^{-1} and 73 ± 12 μJy beam^{-1}, respectively, where the errors comprise both the r.m.s. noise uncertainty and a 10% calibration error, added in quadrature. The r.m.s. noise uncertainties are 9 μJy beam^{-1} and 10 μJy beam^{-1}, hence the detections have a significance of 9.4 and 7.3σ confidence, respectively. No significant emission above the 3σ r.m.s. level (σ =13 μJy beam^{-1}) was reported in the third epoch. The data are shown in Fig. 2 as blue squares.

The upper limits for the flux densities in the radio band were taken with 3σ confidence level. The full list of radio observations is given in Table 1.

3.2. Optical

At 1.4 and 2.2 days post-burst, we clearly detected the optical afterglow in both i and z bands at $\alpha = 23^{\rm h}37^{\rm m}16.43^{\rm s}$, $\delta = +53°24'56.6''$ (J2000; uncertainty = 0.2″). In addition, we detected the host galaxy at $\alpha = 23^{\rm h}37^{\rm m}16.48^{\rm s}$, $\delta = +53°24'54.6''$ (J2000; uncertainty = 0.2″).

The optical light curve is shown in Fig. 2: g-band data from Belkin et al. (2020b, green hexagons), Grossan et al. (2020, green dots) and Ackley et al. (2020, green circles); r-band data from Belkin et al. (2020a, red pentagons), Belkin et al. (2020b, red stars), Zhu et al. (2020a,b, red hexagons), Moskvitin et al. (2020, red diamonds), Grossan et al. (2020, thin red diamonds), Kumar et al. (2020b, red plus), Pozanenko et al. (2020, red circles); i-band data from Grossan et al. (2020, purple squares) and our MMT/Binospec observations (purple circles); our z-band MMT/Binospec observations (brown circles).

The emission peaked between 200 and 300 s after the GRB trigger, reaching a maximum of R∼16.5 mag (Jelinek et al. 2020; Zhu et al. 2020a). Between 0.1 and 3 days our light curve follows a power law $F(t) \propto t^{-0.84\pm0.06}$, which is consistent with previous results in the GCNs (Pozanenko et al. 2020). Remarkably, a type Ic-BL supernova (SN) contribution can be seen between 3 and 20 days after the burst (Pozanenko et al. 2020; Rossi et al. 2021), which corroborates the long-duration nature of this burst.

3.3. X-rays

The *Swift*/XRT light curve was further analysed by splitting the last two observations in four time intervals. We retrieved the XRT spectral files from the online archive[7] and analyse them with the public software XSPEC V12.10.1F, assuming a simple power-law model. The `tbabs` model for the Galactic absorption and the `ztbabs` model for the host galaxy absorption, adopting the source redshift $z = 0.426$, are used in the fitting procedure. The absorption parameters are fixed to the values reported by the *Swift* website for this burst, namely $N_{\rm H,gal} = 3.6 \times 10^{21}$ atoms cm^{-2} (Kalberla et al. 2005; Willingale et al. 2013) and $N_{\rm H,intr} = 5 \times 10^{21}$ atoms cm^{-2}. Leaving the normalisation and the photon index of the power-law free to vary, we find integrated fluxes consistent with those reported on the *Swift* website.

From our two epochs of *Chandra* observations we find 0.5–7 keV source count rates of $(4.07 \pm 0.38) \times 10^{-3}$ cts s^{-1} and $(3.11 \pm 0.29) \times 10^{-3}$ cts s^{-1}. In a combined spectral fit of both *Chandra* epochs and the late XRT observations (>10 days), the data are well modelled (cstat/dof = 600/1808) by an absorbed power law of the form POWERLAW*TBABS*ZTBABS (Wilms et al. 2000) with a photon index of $\Gamma = 2.10 \pm 0.13$. The intrinsic absorption column is fixed to $N_{\rm H,intr} = 5 \times 10^{21}$ atoms cm^{-2} at $z = 0.426$ over the Galactic value of $N_{\rm H,gal} = 3.6 \times 10^{21}$ atoms cm^{-2} (Kalberla et al. 2005; Willingale et al. 2013) to match those reported on the UKSSDC. From this, we derived unabsorbed 0.3–10 keV fluxes of $(1.26 \pm 0.05) \times 10^{-13}$ erg cm^{-2} s^{-1} at 8.4 days and $(1.10 \pm 0.04) \times 10^{-13}$ erg cm^{-2} s^{-1} at 13.6 days.

The X-ray light curve is shown in Fig. 2 for the *Swift*/XRT public data (dark blue circles) and our *Chandra* observations (dark blue squares). For the *Swift*/XRT light curve, we included the results from the SWIFT BURST ANALYZER up to ∼0.12 days, and from that epoch on we used our re-analysis of the last two observations. Our XRT analysis suggests that the light curve can be fitted with a power law with index $F^{-1.1\pm0.3}$ between 0.04 and 0.71 days post-burst, which is shallower but still consistent with the previous analysis from D'Ai et al. (2020). However, the subsequent detections at 8.4 and 13.6 days with *Chandra* show a respective flux ∼6 and 8 times higher than expected from extrapolating the earlier XRT light curve, and the increased flux is further confirmed by the late time (∼20 days after the burst) *Swift*/XRT follow-up (D'Elia & Swift Team 2020).

4. Broadband modelling

The multi-wavelength afterglow synchrotron emission of a GRB seen on-axis can be studied through a standard model (see e.g.

[7] https://www.swift.ac.uk/xrt_spectra

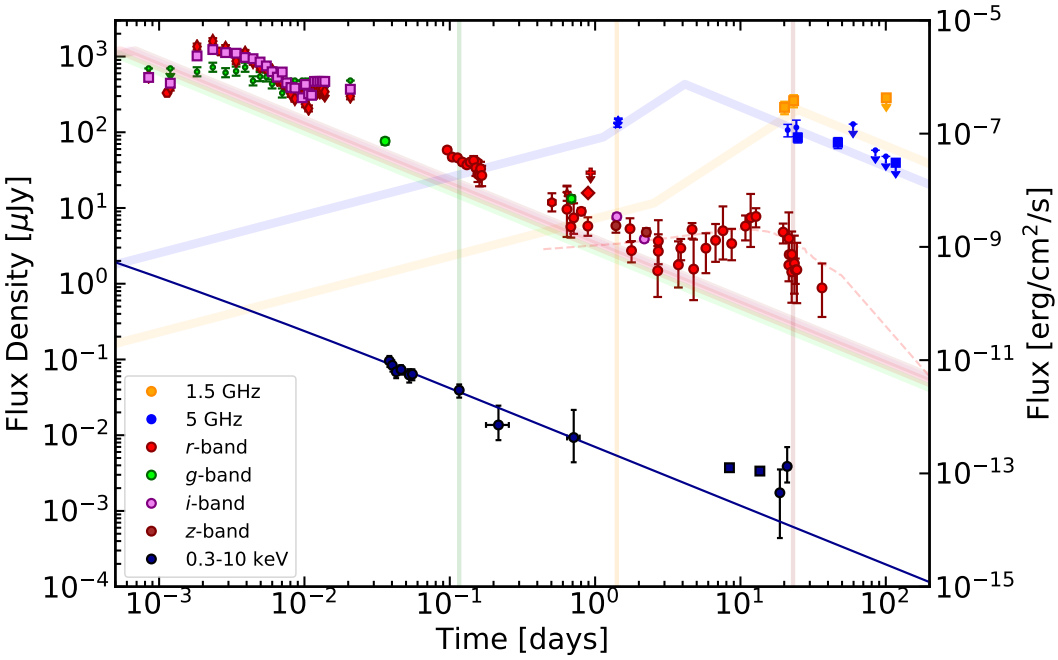

Fig. 2. Multi-wavelength afterglow light curves (see Sect. 3). For each band, the light curves predicted by the standard model with ν_{sa} = 13 GHz, ν_m = 6 GHz, $\nu_c = 2 \times 10^7$ GHz, F_m = 800 μJy, and p = 2.05 at 1 day for a homogeneous surrounding medium are shown: 1.5 GHz (orange); 5 GHz (blue); r, g, i, and z bands (red, lime, violet, and brown, respectively); integrated X-ray light curve (dark blue). The green, orange, and brown vertical lines pinpoint the epochs of the spectra at 0.12, 1.41, and 23 days, respectively (see also Fig. 3). The dashed line shows a simple model for the SN contribution in the r band (see Sect. 5.1).

Granot & Sari 2002; Zhang & Mészáros 2004). First, assuming that the flux density can be parametrised as $F \propto \nu^{\beta} t^{\alpha}$, the spectrum can be fitted with several power law segments, which join at specific break frequencies: (i) the self-absorption frequency ν_{sa}, (ii) the maximum frequency ν_m, and (iii) the cooling frequency ν_c. The other parameters needed to build the spectrum are (iv) the maximum flux density F_m and (v) the electron distribution index p. Once we have determined these quantities and their temporal evolution, the multi-wavelength light curves are constrained. For this work we use the relations provided by Granot & Sari (2002), and throughout the paper we consider two possible density profiles for the circumburst medium: a wind-like profile $\rho = Ar^{-2}$, which is naturally expected if the progenitor is a massive star collapsing into a BH or a NS, and a homogeneous surrounding medium ρ = const, which can be ascribed either to the canonical ISM or to a wind bubble shocked against the ISM (Aksulu et al. 2022). Hereafter we use the term ISM for a homogeneous profile indiscriminately.

We note that in our modelling we do not include the description of the coasting phase, the contribution from the RS, or the late time SN emission. A more sophisticated modelling that comprises the RS contribution would introduce more parameters; if frequent observations are available around the epoch at which the RS is supposed to prevail (at about 1 day in the radio band; see e.g. Rhodes et al. 2020a) these parameters can be constrained. With only one detection in the C band before 20 days post-burst, we could not constrain the parameters. In the optical, the emission before 0.01 days shows a bump that could be due to a possible RS contribution, while after 3 days the SN emission becomes dominant (Pozanenko et al. 2020; Rossi et al. 2021), hence the prediction of the modelling should be considered only from about 0.01 to 3 days post-burst in this band.

To derive the modelling light curves, we performed a comparison of the simplified afterglow prescription with the available data, changing the above-mentioned parameters to get as close as possible to the observed multi-wavelength light curves and to reproduce the afterglow spectrum at three sampling epochs, namely 0.12, 1.41, and 23 days after the GRB trigger (see Fig. 3).

4.1. ISM profile

For the ISM profile we built the spectrum at 0.12 days, with the optical r band from Pozanenko et al. (2020) and the XRT detections at 1.41 days with the VLA detection (see Sect. 3) and our optical i- and z-band observations, and the spectrum at 23 days with our radio detection at 1.5 and 5 GHz, the optical r band from Pozanenko et al. (2020), and the last XRT detection (Fig. 3). From the spectra and the multi-wavelength light curves we constrain the parameter space as follows. First, from the spectral index $\beta = 2.3 \pm 0.1$ derived with the VLA data we cannot discern whether the emission at 6 GHz lies in the ν^2 or $\nu^{5/2}$ portion of the spectrum at 1.41 days, and therefore we consider three different cases. At this epoch it could be that (i) 6 GHz < ν_{sa} < ν_m, (ii) ν_m < 6 GHz < ν_{sa}, or (iii) 6 GHz < $\nu_m \leq \nu_{sa}$. Moreover, at 23 days the spectral slope between 1.5 GHz and 5 GHz is reversed, meaning that the flux density is decreasing with the frequency, and hence we expect that $\nu_m < \nu_{sa} <$ 1.5 GHz. Finally, at 23 days the optical emission is dominated by the SN, hence we consider the optical detections as upper limits. To build the modelling light curves and spectra we derive the break frequencies, the p value, and the maximum flux density F_m at 1 day, in order to simplify the equations from Granot & Sari (2002).

(i) If 6 GHz < ν_{sa} < ν_m, since ν_m > 6 GHz at 1.41 days, $\nu_m \propto t^{-3/2}$ and ν_{sa} is constant in time, to avoid ν_m crossing ν_{sa} before 1.41 days we impose ν_m > 15 GHz and ν_{sa} > 9 GHz at 1 day. However, once ν_m crosses ν_{sa}, $\nu_{sa} \propto t^{-(3p+2)/2(p+4)}$. Therefore at 1 day ν_{sa} < 13 GHz, otherwise at 23 days ν_{sa} > 1.5 GHz, and consequently ν_m < 24 GHz (otherwise it does not cross ν_{sa} before 23 days). At 1 day the flux density at ν_m is found to be 500 μJy < F_m < 600 μJy. With a lower F_m we underestimate the emission at 5 GHz observed with EVN, while with a higher flux we overestimate the e-MERLIN detections at the same frequency. With the slope of the optical light curve we can constrain the p value: since the light curve shows a clear slope that can be described by a single power law between 0.01 and 3 days, ν_m < optical < ν_c and $F \propto t^{3(1-p)/4}$ in this regime. Finally, the X-ray integrated light curve allows us to further constrain

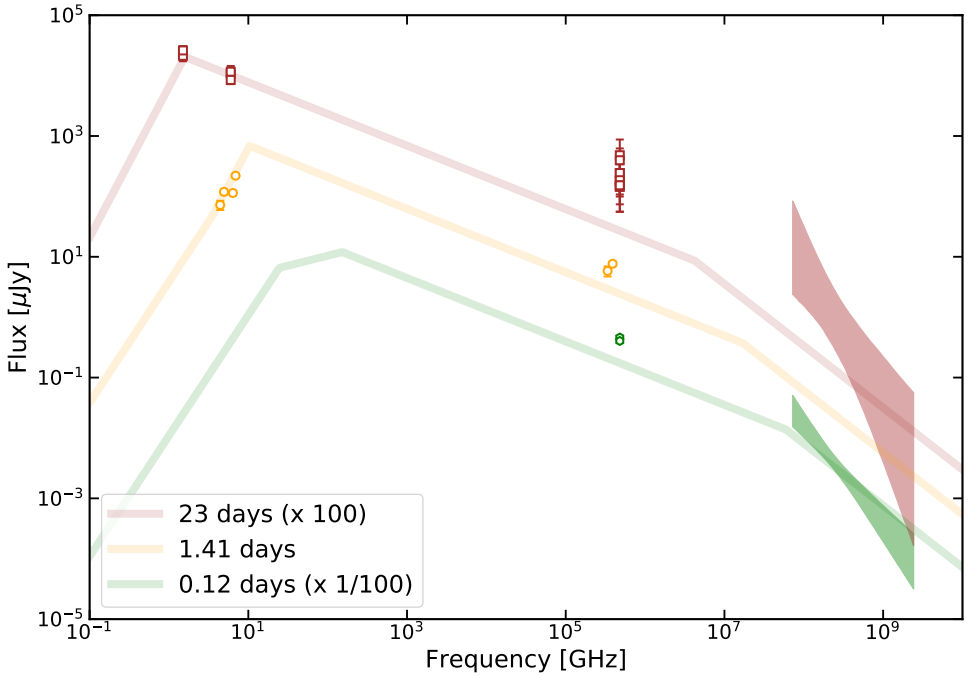

Fig. 3. Spectra at 0.12 (green), 1.41 (orange), and 23 (brown) days after the GRB onset for a homogeneous surrounding medium with ν_{sa} = 13 GHz, ν_m = 6 GHz, $\nu_c = 2 \times 10^7$ GHz, F_m = 800 μJy, and p = 2.05 at 1 day. Spectrum at 0.12 days: optical observations from Pozanenko et al. (2020) and XRT butterfly plot. Spectrum at 1.41 days: our VLA and MMT detections. Spectrum at 23 days: our 1.5 and 5 GHz observations, optical data from Pozanenko et al. (2020) and the XRT butterfly plot; the optical emission is dominated by the SN component.

p and determine ν_c: for $\nu < \nu_c$ we have $F \propto t^{3(1-p)/4}$, while for $\nu > \nu_c$ we have $F \propto t^{(2-3p)/4}$; hence, the sooner ν_c crosses the X-ray band, the fainter the detected emission will be. In summary, to reproduce both the spectra and the light curves we find that 9 GHz $< \nu_{sa} <$ 13 GHz, 15 GHz $< \nu_m <$ 24 GHz, 5×10^6 GHz $< \nu_c < 10^8$ GHz, 500 μJy $< F_m <$ 600 μJy and $2.01 < p < 2.10$ at 1 day.

(ii) If $\nu_m <$ 6 GHz $< \nu_{sa}$ at 1.41 days, since $\nu_{sa} \propto t^{-(3p+2)/2(p+4)}$, we impose that $\nu_{sa} >$ 10 GHz at 1 day; moreover, $\nu_{sa} <$ 18 GHz at 1 day, otherwise at 23 days $\nu_{sa} >$ 2 GHz and our detections at 1.5 GHz would lie in the $\nu^{5/2}$ portion of the spectrum and the emission at 5 GHz would be overestimated. To reproduce the spectra and the light curves we find that the range for ν_{sa} is further constrained to 13 GHz $< \nu_{sa} <$ 16 GHz. Since at 1.41 days $\nu_m \leq$ 4 GHz (otherwise the lowest end of the bandwidth of the VLA detection would be underestimated), at 1 day $\nu_m \leq$ 7 GHz. Finally, with the same argument presented in case (i), we find that at 1 day 6×10^6 GHz $< \nu_c < 10^8$ GHz, 800 μJy $< F_m <$ 1 mJy and $2.01 < p < 2.20$. We note that in this case F_m refers to the flux density at ν_{sa}.

(iii) If 6 GHz $< \nu_m \leq \nu_{sa}$ at 1.41 days, we can have both 6 GHz $< \nu_m < \nu_{sa}$ and 6 GHz $< \nu_{sa} < \nu_m$ at 1 day. Considering both these sub-cases, since $\nu_m \propto t^{-3/2}$, at 1 day $\nu_m >$ 13 GHz, otherwise at 1.41 days $\nu_m <$ 8 GHz and it would lie too close to the highest end of the bandwidth of the VLA detection to reproduce the spectrum; conversely, if at 1 day $\nu_m >$ 18 GHz, we cannot reproduce the light curve in the C band because the detections at 6 GHz with the VLA are underestimated, while e-MERLIN and EVN observations are overestimated. Since at 1.41 days $\nu_{sa} \geq \nu_m$, we find that 13 GHz $< \nu_{sa} <$ 18 GHz (for larger values we cannot reproduce the C band light curve). Once again, with the same argument presented in case (i), we derived 5×10^6 GHz $< \nu_c < 2 \times 10^8$ GHz, 630 μJy $< F <$ 1 mJy and $2.01 < p < 2.20$ at 1 day. In this case F_m refers to the flux density of ν_{sa} or ν_m for the two sub-cases. We note that these ranges for the parameters are the superposition of the ranges derived for the two sub-cases.

Table 2. Constraints on the model parameters at 1 day for a homogeneous circumburst medium.

Parameter	Range
ν_{sa}	9–18 GHz
ν_m	≤7 GHz ⋃ 13–24 GHz
ν_c	5×10^6–2×10^8 GHz
F_m	0.5–1 mJy
p	2.01–2.20

In Table 2, we report our results for the parameter space at 1 day. The model light curves for the ISM profile are shown in Fig. 2 for ν_{sa} = 13 GHz, ν_m = 6 GHz, $\nu_c = 2\times10^7$ GHz, F_m = 800 μJy at 1 day, and an electron distribution index p = 2.05. The 1.5 GHz and the 5 GHz light curve are displayed in orange and blue, respectively; the r, g, i, and z bands are in red, lime, violet, and brown, respectively; the X-ray light curve is displayed in dark blue. Although this modelling provides a satisfactory description of the multi-wavelength light curves, the optical light curve contains the already discussed features in addition to the forward shock emission: before 0.01 days there is a bump which could be due to a possible RS contribution, while after three days the SN emission becomes dominant (Pozanenko et al. 2020; Rossi et al. 2021).

4.2. Wind-like profile

For the wind-like profile we first tried to reproduce the optical and X-ray data, finding that ν_{sa} = 1 GHz, ν_m = 30 GHz, $\nu_c = 2\times10^7$ GHz, F_m = 200 μJy at 1 day, and the electron distribution index p = 2.01. Since this model conspicuously failed to reproduce the radio detections and the optical slope, we tried to reproduce the radio light curve at 5 GHz first, and we found that ν_{sa} = 4 GHz, $\nu_m = 10^3$ GHz, $\nu_c = 2\times10^7$ GHz, F_m = 600 μJy at 1 day, and the electron distribution index p = 2.01. Neither of

these models reproduces the optical slope, and the second model fails to reproduce the X-ray emission. Different choices of the parameters in the wind-like scenario provide even poorer fits. We can therefore conclude that the modelling provided by the ISM provides the best agreement with the data, and we consider it hereafter. We note that this further corroborates the need of X-ray, optical, and radio observations in order to break the degeneracy in the afterglow modelling, as with only two of them data can be misinterpreted.

4.3. Intrinsic host galaxy extinction

As pointed out by Kann et al. (2006), the intrinsic host galaxy extinction can be relevant in the optical/NIR. By changing the model parameters, we tried overestimating the optical emission and, from the discrepancy between the observed and the modelled optical flux densities, the contribution due to the intrinsic host galaxy absorption can be estimated. However, our modelling light curves and spectra cannot predict values for the flux density that are larger than those observed in the optical data. Moreover, by changing the maximum flux density and the p-value, we cannot reproduce the observed light curves in the radio band. As our modelling light curve already underestimates the afterglow optical emission (see Fig. 3), by adding the intrinsic host galaxy extinction the discrepancy would increase. Therefore the only constraint we can put on the intrinsic host galaxy absorption is that it is negligible, if we assume that the model is correct. Although more sophisticated models could take into account this further correction, this is beyond the goals of this work.

5. Discussion

Once the free parameters ν_{sa}, ν_m, ν_c, F_m, and p are constrained, we can exploit the relations provided by Granot & Sari (2002) to derive the global and microphysical parameters of the jet: the isotropic kinetic energy E, the density of the medium that surrounds the progenitor n, the fraction of internal energy retained by the magnetic field ϵ_B, and the fraction of internal energy retained by the electrons ϵ_e. From the conservation of energy, we know that $\epsilon_e \leq 1$, $\epsilon_B \leq 1$, and $\epsilon_e + \epsilon_B \leq 1$. A further constraint is given by the VHE emission; if we consider the sub-TeV emission to be due to the SSC from the relativistic electrons, then $\epsilon_e \geq \epsilon_B$ (Sari & Esin 2001; Zhang & Mészáros 2001). If we try to solve the equations from Granot & Sari (2002), the inferred parameters violate the conservation of energy (i.e. $\epsilon_e + \epsilon_B \geq 1$); however, these values are determined under the implicit assumption that all the electrons that are swept up by the forward shocks are accelerated, while this is expected to be true only for a fraction f of them. As shown by Eichler & Waxman (2005), if $m_e/m_p \leq f \leq 1$ the observed emission does not change when scaling the parameters as follows: $E \rightarrow E/f$, $\epsilon_e \rightarrow \epsilon_e f$, $\epsilon_B \rightarrow \epsilon_B f$, $n \rightarrow n/f$ (van der Horst et al. 2014). In order to find the solutions, we make E and ϵ_e vary within physically reasonable ranges (i.e. 10^{50} erg $\leq E \leq 10^{55}$ erg and $10^{-4} \leq \epsilon_e \leq 1$), and we subsequently calculate ϵ_B and n using the inferred break frequencies, F_m and p. Finally, we apply the constraints given by the conservation of energy and the sub-TeV emission. The final solutions are listed in the second column of Table 3.

Furthermore, since we expect ϵ_e to be of the order of 0.1 from numerical simulations (Sironi et al. 2013, and references therein), we provide the full set of inferred values for the $0.05 \leq \epsilon_e \leq 0.15$ case in the second column of Table 4. We find that the isotropic kinetic energy goes from 3×10^{50} to 10^{55} erg. If we consider the isotropic-equivalent energy derived by Minaev & Pozanenko (2020) from the prompt emission, we can roughly estimate the efficiency of the prompt emission as $\eta = E_{iso}/(E + E_{iso})$. We estimate that $\eta \simeq 10^{-3}$–27%.

To discuss these values in a broader context we consider a recent work by Aksulu et al. (2022), who examined 26 GRBs with well-sampled broadband data sets. The authors found that ϵ_B ranges from $\approx 2.6 \times 10^{-6}$ (GRB 030329) to ≈ 0.91 (GRB 130907A) for those GRBs that can be described with an ISM profile (hereafter ISM Sample), and 3 out of 13 GRBs have $\epsilon_B \geq 0.5$; for ϵ_e they found a range between ≈ 0.14 (GRB 090328) and ≈ 0.89 (GRB 010222); finally, n goes from $\approx 5 \times 10^{-3}$ (GRB 010222) to $\approx 390\,\mathrm{cm}^{-3}$ (GRB 030329).

We then consider long GRBs with a claimed RS detection (in X-rays, optical, and/or radio) whose multi-wavelength light curves can be aptly described with an ISM profile (hereafter RS Sample): GRB 990123, 021004, 021211, 060908, 061126, 080319B, 090102, and 090424 (Japelj et al. 2014); GRB 130427A (Perley et al. 2014); GRB 160509A (Laskar et al. 2016); GRB 160625B (Alexander et al. 2017); GRB 161219B (Laskar et al. 2018); GRB 180720B (Wang et al. 2019); GRB 190829A (Rhodes et al. 2020a). The circumburst density for the GRBs of the RS Sample goes from $\approx 5 \times 10^{-5}\,\mathrm{cm}^{-3}$ for GRB 160625B to $\approx 360\,\mathrm{cm}^{-3}$ for GRB 090201, while ϵ_e ranges from $\approx 4 \times 10^{-4}$ for GRB 090102 to ≈ 0.93 for 161219B

Table 3. Global and microphysical parameters for GRB 201015A in the ISM scenario.

Parameter	Value	Median	
		ISM sample	RS sample
E_{52}/erg	0.03–10^3	12	20
ϵ_e	10^{-4}–0.99	0.32	0.104
ϵ_B	8×10^{-7}–0.05	2.7×10^{-2}	1.4×10^{-4}
$n\,\mathrm{cm}^{-3}$	0.4–2×10^4	1.5	2.15
f	0.01–1.00		

Notes. The parameter name and the inferred value are listed in the first and second column, respectively. The median of the sample by Aksulu et al. (2022) for those bursts that can be reproduced with an ISM profile is reported in the third column (ISM sample), while the median for the sample of bursts with a claimed reverse shock component is reported in the fourth column (RS sample).

Table 4. Global and microphysical parameters for GRB 201015A in the ISM scenario if $0.05 \leq \epsilon_e \leq 0.15$.

Parameter	Value	Median	
		ISM sample	RS sample
E_{52}/erg	0.03–14	12	20
ϵ_e	0.05–0.15	0.32	0.104
ϵ_B	1.5×10^{-6}–0.05	2.7×10^{-2}	1.4×10^{-4}
$n\,\mathrm{cm}^{-3}$	0.4–10^4	1.5	2.15
f	0.02–1.00		

Notes. The parameter name and the inferred value are listed in the first and second column, respectively. The median of the sample by Aksulu et al. (2022) for those bursts that can be reproduced with an ISM profile is reported in the third column (ISM sample), while the median for the sample of bursts with a claimed reverse shock component is reported in the fourth column (RS sample).

and ϵ_B goes from $\approx 2 \times 10^{-5}$ for GRB 090102 to ≈ 0.11 for GRB 160509A. The values we infer for GRB 201015A are therefore consistent with those found in the ISM and RS samples, even though the surrounding density is generally higher.

Finally, we consider three GRBs that have been detected at VHE: GRB 180720B, GRB 190114C, and GRB 190829A. For these bursts ϵ_e goes from 0.02 (GRB 190114C; Misra et al. 2021) to 0.1 (GRB 180720B; Wang et al. 2019); ϵ_B goes from 4.7×10^{-5} (GRB 190114C; Misra et al. 2021) to 10^{-4} (GRB 180720B; Wang et al. 2019); and the surrounding medium density n goes from 0.1 (GRB 180720B; Wang et al. 2019) to 23 (GRB 190114C; Misra et al. 2021). These values are consistent with those we derive for GRB 201015A in this work.

From the maximum flux density F_m at 8.5 GHz we calculate the luminosity L of the afterglow with $L = F_m 4\pi d_l^2 (1+z)^{\beta-\alpha-1}$ (Chandra & Frail 2012), where d_l is the luminosity distance in cm, F_m is expressed in erg s^{-1} cm^{-2} Hz^{-1}, z is the redshift, and $\alpha = \beta = 0$ since the peak in the light curve is also a peak in the spectrum. We find that $L \simeq 3.5 \times 10^{30}$ erg s^{-1} Hz^{-1} at 1.9 days, which is slightly below the average value for radio-detected GRB afterglows (Chandra & Frail 2012). Finally, the maximum luminosity $L \simeq 5.4 \times 10^{30}$ erg s^{-1} Hz^{-1} at 15.7 GHz at 0.8 days is consistent with the radio luminosity previously found for the other GRBs detected at VHE (Rhodes et al. 2020a).

We note that the allowed ranges inferred for the microphysical and global parameters of GRB 201015A are too large to pinpoint any possible deviation of this burst from the samples we used, and hence to derive important information on the production of VHE photons in GRBs. Moreover, a population study is still hindered by the paucity of GRBs detected at VHE and their proximity ($z < 1.1$), which could lead to a strong bias. A larger and more complete sample is therefore needed. On the other hand, the fact that we cannot flag any possible deviation from the mentioned samples could be consistent with the VHE GRBs being drawn from the same parent population as the other radio-detected long GRBs (Rhodes et al. 2020a).

5.1. Additional emission components

It is worth noting that a refined model could possibly be obtained by including the RS component, whose prescription could explain the bump and the observed excess in the optical emission before 0.01 days. All the GRBs with a confirmed VHE emission were in fact successfully modelled once a RS component was included: GRB 180720B (Fraija et al. 2019; Wang et al. 2019), GRB 190114C (Laskar et al. 2019b), GRB 190829A (Rhodes et al. 2020a).

Concerning the SN emission, if we take the emission of SN1998bw in the r band (Galama et al. 1998), de-absorb the flux density using $A_V = 0.2$ (Galama et al. 1998), and move the SN to $z = 0.426$ and seven days earlier, we find that its light curve is consistent with that observed for GRB 201015A after three days from the burst (see Fig. 2, dashed line). This further strengthens the SN origin of the bump observed around ten days post-burst.

Finally, we suggest that a transition between the wind-like profile and the ISM profile at around 0.1–0.2 days could possibly explain the change in slope observed in the X-ray light curve after ~0.2 days (see e.g. Kamble et al. 2007; Veres et al. 2015). The optical slope between 0.03 and 0.2 days follows a power law $F \propto t^{-1.1 \pm 0.2}$, which is consistent with the prediction from a model with a wind-like profile, namely $F \propto t^{-1.3}$, if the optical lies between ν_m and ν_c. The prediction for the fireball model with a homogeneous circumburst medium is $F \propto t^{-0.8}$, which is still consistent but shallower.

5.2. High-resolution observations

To measure the expansion or the proper motion of the outflow, a high signal-to-noise ratio is required as it allows both a follow-up of the afterglow up to later times and a smaller uncertainty on the position of the detected source (Taylor et al. 1999). While we achieved a milliarcsecond angular resolution with EVN, we could not pinpoint any displacement of the centroid (off-axis GRB, Mooley et al. 2018; Ghirlanda et al. 2019) nor an expansion of the source (on-axis GRB, Taylor et al. 2004).

The position of the afterglow in the two detections with EVN is consistent within the uncertainties (i.e. $\Delta\alpha = 0.2$ mas and $\Delta\delta = 0.3$ mas). At $z = 0.426$, the centroid displacement before 47 days post-burst is therefore smaller than 1.1 pc in right ascension and 1.7 pc in declination; assuming that the burst is observed at the viewing angle θ that maximises the apparent velocity $\beta_{app} = \Gamma$ (i.e. $\theta \sim \beta_{app}^{-1}$), we derive a Lorentz factor upper limit of $\Gamma_\alpha \leq 40$ in right ascension and $\Gamma_\delta \leq 61$ in declination. Considering the previous outstanding burst for which a proper motion was observed (i.e. GRB 170817A at $z = 0.0093$), a displacement of the same magnitude as that of GRB 170817A would have been seen as 0.08 mas at $z = 0.426$ after ~207 days post-burst.

On the other hand, if the GRB is seen on-axis, by taking the minor axis of the beam we constrain the size of the afterglow to be $\leq$5 pc and $\leq$16 pc at 25 and 47 days, respectively. Considering the only case for which the expansion was confirmed (i.e. GRB 030329 at $z = 0.1685$), an expansion of the same magnitude as that of GRB 030329 would have been seen as 0.09 mas at $z = 0.426$ after ~80 days post-burst.

Since our best resolution with EVN is 1.8 mas × 0.9 mas, we would have detected such an expansion or displacement if (i) the size of the beam had not changed in later observations; (ii) the afterglow had been observable and detectable with a signal-to-noise ratio higher than 10 for about 200 days and 80 days in the case of displacement and expansion, respectively; and (iii) the displacement or expansion had occurred along the coordinate corresponding to the minor axis of the beam.

Conversely, considering the worst resolution reached with our VLBI observations, 3.1 mas × 3.6 mas, we would have pinpointed these effects if the afterglow had been detectable for about 800 days or 320 days in the case of proper motion and expansion, respectively, so that the measurements to be performed would have been of the order of 0.3 mas.

5.3. Host galaxy

The host galaxy was first pinpointed by Belkin et al. (2020a) and subsequently confirmed by Rastinejad et al. (2020) and Rossi et al. (2021), who found a magnitude $r = 22.9 \pm 0.2$.

With the MMT observations, we derive the position of the host of $\alpha = 23^h37^m16.4757^s$, $\delta = +53°24'54.626''$ (J2000; uncertainty = 0.235″); this is found to be 1.86″ from the source observed at 1.5 GHz, which corresponds to roughly 10 kpc at $z = 0.426$. The uncertainty in the radio position at 1.5 GHz is 0.03″, which is ~170 pc, and therefore we can state that the emission observed at 1.5 GHz is consistent with being generated by the afterglow. Moreover, as the beam size at 1.5 GHz is roughly 0.18″× 0.12″, the emitting region should be of the order of 1 kpc × 0.7 kpc; if the detected emission were caused by a very active star-forming region, we would have observed a stable emission in the optical at the same position instead of a transient event.

A safe discrimination between the galactic contamination and the proper afterglow emission at 1.5 GHz could also be

achieved with a higher resolution and an improved sensitivity in late epochs in order to obtain better constraints on the light curve. While the former requirement is provided by VLBI observations, the latter is reached with the Pathfinders of the Square Kilometre Array (SKA): the Meer Karoo Array Telescope (MeerKAT; see e.g. Rhodes et al. 2020a) and the Australian Square Kilometre Array Pathfinder (ASKAP). Moreover, a better sensitivity allows the detection of possible late time jet breaks, and therefore the measurement of the jet opening angle.

6. Conclusions

GRB 201015A was a nearby ($z = 0.426$; de Ugarte Postigo et al. 2020; Izzo et al. 2020) long-duration GRB discovered on 2020 October 15 by *Swift*/BAT (D'Elia et al. 2020). Its long-lasting afterglow emission has been observed from γ rays down to radio bands; it is claimed to be the fifth GRB ever detected at VHE energies (Blanch et al. 2020a; Suda et al. 2021).

We performed a radio follow-up with the VLA, e-MERLIN, and EVN at 1.5 and 5 GHz over 12 epochs from 1.4 to 117 days after the GRB onset. At 5 GHz we detected a point-like source consistent with the afterglow position on 2020 October 17; 2020 November 5, 8, and 9; and 2020 December 1; conversely, on 2020 December 14, 2021 January 8 and 23, and 2021 February 9 no source was detected. At 1.5 GHz we detected a point-like source on 2020 November 4 and 7, while on 2021 January 24 no source was detected.

We observed and detected the afterglow of GRB 201015A also in X-rays with *Chandra* (8.4 and 13.6 days post-burst) and in the optical with MMT (1.4 and 2.2 days post-burst). Finally, we collected public X-ray data from *Swift*/XRT and optical data from the GCN Circulars Archive. We built multi-wavelength light curves and three spectra at 0.12, 1.41, and 23 days post-burst, and we exploited the standard model provided by Granot & Sari (2002) for a sharp-edged jet seen on-axis to constrain the global and microphysical parameters of the outflow. We find that the observed light curves can be reproduced with a homogeneous circumburst medium profile, and that the parameters we derived for GRB 201015A are consistent with those previously found in the literature for other GRBs, even though we caution that a fully reliable modelling will require a proper characterisation of the VHE detection, which is unavailable at present.

Despite the high angular resolution we achieved with the EVN observations, we could not pinpoint any change in the afterglow position. If the GRB is seen slightly off-axis, we constrain the proper motion of the outflow to be smaller than 1.1 pc in right ascension and 1.7 pc in declination before 47 days post-burst. This proper motion corresponds to a Lorentz factor upper limit of $\Gamma_\alpha \leq 40$ in right ascension and $\Gamma_\delta \leq 61$ in declination, if we assume that the GRB is seen at the viewing angle θ which maximises the apparent velocity $\beta_{\rm app}$ (i.e. $\theta \sim \beta_{\rm app}^{-1}$). Conversely, if the GRB is seen on-axis, we find that the size of the afterglow is $\leq$5 pc and $\leq$16 pc at 25 and 47 days, respectively.

We note that the bump before 0.01 days post-burst in the optical light curve could be explained by an RS component. On the other hand, we find that the *Chandra* and the last *Swift*/XRT detections are brighter than expected from the model and from the extrapolation of the previous data points. Even though further observations are needed, a late time central engine activity or a transition from a wind-like profile to a homogeneous surrounding medium at early times could possibly explain the change in the slope of the X-ray light curve.

Acknowledgements. The authors would like to thank the anonymous referee for their helpful comments. e-MERLIN is a National Facility operated by the University of Manchester at Jodrell Bank Observatory on behalf of STFC, part of UK Research and Innovation. The European VLBI Network is a joint facility of independent European, African, Asian, and North American radio astronomy institutes. Scientific results from data presented in this publication are derived from the following EVN project code: RM016. We thank the directors and staff of all the EVN telescopes for making this target of opportunity observation possible. The National Radio Astronomy Observatory is a facility of the National Science Foundation operated under cooperative agreement by Associated Universities, Inc. MMT Observatory access was supported by Northwestern University and the Center for Interdisciplinary Exploration and Research in Astrophysics (CIERA). The scientific results reported in this article are based in part on observations made by the *Chandra* X-ray Observatory (PI: Gompertz; project code: 22400511). This research has made use of software provided by the *Chandra* X-ray Center (CXC) in the application packages CIAO and Sherpa. BM and JMP acknowledge financial support from the State Agency for Research of the Spanish Ministry of Science and Innovation under grant PID2019-105510GB-C31 and through the Unit of Excellence María de Maeztu 2020-2023 award to the Institute of Cosmos Sciences (CEX2019-000918-M). AJL has received funding from the European Research Council (ERC) under the European Union's Seventh Framework Programme (FP7-2007–2013) (Grant agreement no. 725246). BPG acknowledges funding from the European Research Council (ERC) under the European Union's Horizon 2020 research and innovation programme (grant agreement no. 948381, PI: Nicholl).

References

Abdalla, H., Adam, R., Aharonian, F., et al. 2019, Nature, 575, 464
Ackley, K., Galloway, D. K., Mong, Y.-L., et al. 2020, GRB Coordinates Network, Circular Service, 28639
Aksulu, M. D., Wijers, R. A. M. J., van Eerten, H. J., et al. 2022, MNRAS, 511, 2848
Alexander, K. D., Laskar, T., Berger, E., et al. 2017, ApJ, 848, 69
Amati, L., Frontera, F., Tavani, M., et al. 2002, A&A, 390, 81
Beasley, A. J., Gordon, D., Peck, A. B., et al. 2002, ApJS, 141, 13
Becker, A. 2015, Astrophysics Source Code Library [record ascl:1504.004]
Belkin, S., Pankov, N., Pozanenko, A., et al. 2020a, GRB Coordinates Network, Circular Service, 28656
Belkin, S., Kim, V., Pozanenko, A., et al. 2020b, GRB Coordinates Network, Circular Service, 28673
Berger, E. 2014, ARA&A, 52, 43
Berger, E., Kulkarni, S. R., & Frail, D. A. 2004, ApJ, 612, 966
Blanch, O., Gaug, M., Noda, K., et al. 2020a, GRB Coordinates Network, Circular Service, 28659
Blanch, O., Longo, F., Berti, A., et al. 2020b, GRB Coordinates Network, Circular Service, 29075
Chambers, K. C., Magnier, E. A., Metcalfe, N., et al. 2016, ArXiv e-prints [arXiv:1612.0556]
Chandra, P., & Frail, D. A. 2012, ApJ, 746, 156
Condon, J. J. 1992, ARA&A, 30, 575
D'Ai, A., Gropp, J. D., Kennea, J. A., et al. 2020, GRB Coordinates Network, Circular Service, 28660
D'Elia, V., & Swift Team 2020, GRB Coordinates Network, Circular Service, 28857
D'Elia, V., Ambrosi, E., Barthelmy, S. D., et al. 2020, GRB Coordinates Network, Circular Service, 28632
de Ugarte Postigo, A., Kann, D. A., Blazek, M., et al. 2020, GRB Coordinates Network, Circular Service, 28649
Drenkhahn, G., & Spruit, H. C. 2002, A&A, 391, 1141
Eichler, D., & Waxman, E. 2005, ApJ, 627, 861
Evans, P. A., Beardmore, A. P., Page, K. L., et al. 2007, A&A, 469, 379
Evans, P. A., Beardmore, A. P., Page, K. L., et al. 2009, MNRAS, 397, 1177
Fletcher, C., Veres, P., & Fermi-GBM Team 2020, GRB Coordinates Network, Circular Service, 28663
Fong, W., Schroeder, G., Rastinejad, J., et al. 2020, GRB Coordinates Network, Circular Service, 28688
Fraija, N., Dichiara, S., Pedreira, A. C. C. do E. S., et al. 2019, ApJ, 885, 29
Fraija, N., Veres, P., Beniamini, P., et al. 2021, ApJ, 918, 12
Frail, D. A., Kulkarni, S. R., Nicastro, L., et al. 1997, Nature, 389, 261
Frail, D. A., Metzger, B. D., Berger, E., et al. 2004, ApJ, 600, 828
Frail, D. A., Soderberg, A. M., Kulkarni, S. R., et al. 2005, ApJ, 619, 994
Galama, T. J., Vreeswijk, P. M., van Paradijs, J., et al. 1998, Nature, 395, 670
Gehrels, N., Ramirez-Ruiz, E., & Fox, D. B. 2009, ARA&A, 47, 567
Geng, J.-J., Dai, Z.-G., Huang, Y.-F., et al. 2018, ApJ, 856, L33
Ghirlanda, G., Salafia, O. S., Paragi, Z., et al. 2019, Science, 363, 968
Giarratana, S., Giroletti, M., Marcote, B., et al. 2020, GRB Coordinates Network, Circular Service, 28939

Gompertz, B., Levan, A., Tanvir, N., et al. 2020, GRB Coordinates Network, Circular Service, 28822
Gordon, D., Jacobs, C., Beasley, A., et al. 2016, AJ, 151, 154
Granot, J., & Sari, R. 2002, ApJ, 568, 820
Greisen, E. W. 2003, Information Handling in Astronomy – Historical Vistas, 109
Grossan, B., Maksut, Z., Kim, A., et al. 2020, GRB Coordinates Network, Circular Service, 28674
H.E.S.S. Collaboration (Abdalla, H., et al.) 2021, Science, 372, 1081
Hinshaw, G., Larson, D., Komatsu, E., et al. 2013, ApJS, 208, 19
Hu, Y.-D., Fernandez-Garcia, E., Castro-Tirado, A. J., et al. 2020, GRB Coordinates Network, Circular Service, 28645
Izzo, L., Malesani, D. B., Zhu, Z. P., et al. 2020, GRB Coordinates Network, Circular Service, 28661
Japelj, J., Kopač, D., Kobayashi, S., et al. 2014, ApJ, 785, 84
Jelinek, M., Strobl, J., Karpov, S., et al. 2020, GRB Coordinates Network, Circular Service, 28664
Jin, Z.-P., Covino, S., Della Valle, M., et al. 2013, ApJ, 774, 114
Kalberla, P. M. W., Burton, W. B., Hartmann, D., et al. 2005, A&A, 440, 775
Kamble, A., Resmi, L., & Misra, K. 2007, ApJ, 664, L5
Kann, D. A., Klose, S., & Zeh, A. 2006, ApJ, 641, 993
Keimpema, A., Kettenis, M. M., Pogrebenko, S. V., et al. 2015, Exper. Astron., 39, 259
Kennea, J. A., Tagliaferri, G., Campana, S., et al. 2020, GRB Coordinates Network, Circular Service, 28635
Kouveliotou, C., Meegan, C. A., Fishman, G. J., et al. 1993, ApJ, 413, L101
Kouveliotou, C., Wijers, R. A. M. J., & Woosley, S. 2012, Gamma-ray Bursts, eds. Chryssa Kouveliotou, Ralph A. M. J. Wijers, Stan Woosley, (Cambridge, UK: Cambridge University Press)
Kumar, P., & Zhang, B. 2015, Phys. Rep., 561, 1
Kumar, H., Sahu, D. K., Gupta, R., et al. 2020a, GRB Coordinates Network, Circular Service, 28680
Kumar, H., Stanzin, U., Bhalerao, V., et al. 2020b, GRB Coordinates Network, Circular Service, 28681
Laskar, T., Alexander, K. D., Berger, E., et al. 2016, ApJ, 833, 88
Laskar, T., Alexander, K. D., Berger, E., et al. 2018, ApJ, 862, 94
Laskar, T., Alexander, K. D., Gill, R., et al. 2019, ApJ, 878, L26
Lipunov, V., Gorbovskoy, E., Kornilov, V., et al. 2020a, GRB Coordinates Network, Circular Service, 28633
Lipunov, V., Gorbovskoy, E., Kornilov, V., et al. 2020b, GRB Coordinates Network, Circular Service, 28634
MAGIC Collaboration, Acciari, V. A., Ansoldi, S., et al. 2019, Nature, 575, 455
Malesani, D. B., de Ugarte Postigo, A., & Pursimo, T. 2020, GRB Coordinates Network, Circular Service, 28637
Marcote, B., Ribó, M., Paredes, J. M., et al. 2020, GRB Coordinates Network, Circular Service, 29028
Markwardt, C. B., Barthelmy, S. D., Cummings, J. R., et al. 2020, GRB Coordinates Network, Circular Service, 28658
Marshall, F. E., D'Elia, V., & Swift/UVOT Team 2020, GRB Coordinates Network, Circular Service, 28662
Mazets, E. P., Golenetskii, S. V., Ilyinskii, V. N., et al. 1981, Ap&SS, 80, 119
McMullin, J. P., Waters, B., Schiebel, D., et al. 2007, Astron. Data Anal. Softw. Syst. XVI, 376, 127
Mészáros, P. 2002, ARA&A, 40, 137
Mészáros, P., & Rees, M. J. 1993, ApJ, 405, 278
Mészáros, P., & Rees, M. J. 1994, MNRAS, 269, L41
Mészáros, P., Rees, M. J., & Papathanassiou, H. 1994, ApJ, 432, 181
Minaev, P., & Pozanenko, A. 2020, GRB Coordinates Network, Circular Service, 28668
Misra, K., Resmi, L., Kann, D. A., et al. 2021, MNRAS, 504, 5685
Monet, D. G., Levine, S. E., Canzian, B., et al. 2003, AJ, 125, 984
Mooley, K. P., Deller, A. T., Gottlieb, O., et al. 2018, Nature, 561, 355
Moskvitin, A. S., Aitov, V. N., & GRB follow-up Team 2020, GRB Coordinates Network, Circular Service, 28721
Norris, J. P., Cline, T. L., Desai, U. D., et al. 1984, Nature, 308, 434
Paczyński, B. 1998, ApJ, 494, L45
Perley, D. A., Cenko, S. B., Corsi, A., et al. 2014, ApJ, 781, 37
Piran, T. 2004, Rev. Mod. Phys., 76, 1143
Pozanenko, A., Belkin, S., Volnova, A., et al. 2020, GRB Coordinates Network, Circular Service, 29033
Pradel, N., Charlot, P., Lestrade, J.-F. 2006, A&A, 452, 1099
Rastinejad, J., Paterson, K., Kilpatrick, C. D., et al. 2020, GRB Coordinates Network, Circular Service, 28676
Rees, M. J., & Mészáros, P. 1992, MNRAS, 258, 41
Rees, M. J., & Mészáros, P. 1994, ApJ, 430, L93
Rhodes, L., Fender, R., Bray, J., et al. 2020, GRB Coordinates Network, Circular Service, 28945
Rhodes, L., van der Horst, A. J., Fender, R., et al. 2020, MNRAS, 496, 3326
Rossi, A., Benetti, S., Palazzi, E., et al. 2021, GRB Coordinates Network, Circular Service, 29306
Salafia, O. S., Ravasio, M. E., Yang, J., et al. 2022, ApJL, 931, L19
Sari, R., & Esin, A. A. 2001, ApJ, 548, 787
Schlafly, E. F., & Finkbeiner, D. P. 2011, ApJ, 737, 103
Selsing, J., Fynbo, J. P. U., Heintz, K. E., et al. 2019, GRB Coordinates Network, Circular Service, 23695
Shepherd, M. C., Pearson, T. J., & Taylor, G. B. 1994, BAAS, 26, 987
Sironi, L., Spitkovsky, A., & Arons, J. 2013, ApJ, 771, 54
Suda, Y., Artero, M., Asano, K., et al. 2021, Proceedings of 37th International Cosmic Ray Conference – PoS(ICRC2021), 395, 797
Taylor, G. B., Carilli, C. L., & Perley, R. A. 1999, Synthesis Imaging in Radio Astronomy II, 180
Taylor, G. B., Frail, D. A., Berger, E., et al. 2004, ApJ, 609, L1
Tody, D. 1993, Astronomical Data Analysis Software and Systems II, 52, 173
Usov, V. V. 1992, Nature, 357, 472
Valeev, A. F., Castro-Tirado, A. J., Hu, Y.-D., et al. 2019, GRB Coordinates Network, Circular Service, 25565
van der Horst, A. J., Paragi, Z., de Bruyn, A. G., et al. 2014, MNRAS, 444, 3151
Veres, P., Corsi, A., Frail, D. A., et al. 2015, ApJ, 810, 31
Vielfaure, J.-B., Izzo, L., Xu, D., et al. 2020, GRB Coordinates Network, Circular Service, 29077
Vreeswijk, P. M., Kann, D. A., Heintz, K. E., et al. 2018, GRB Coordinates Network, Circular Service, 22996
Wang, X.-Y., Liu, R.-Y., Zhang, H.-M., et al. 2019, ApJ, 884, 117
Woosley, S. E. 1993, ApJ, 405, 273
Willingale, R., Starling, R. L. C., Beardmore, A. P., et al. 2013, MNRAS, 431, 394
Wilms, J., Allen, A., & McCray, R. 2000, ApJ, 542, 914
Woosley, S. E., & Heger, A. 2006, ApJ, 637, 914
Zhang, B., & Mészáros, P. 2001, ApJ, 559, 110
Zhang, B., & Mészáros, P. 2004, Int. J. Mod. Phys. A, 19, 2385
Zhang, W., & MacFadyen, A. 2009, ApJ, 698, 1261
Zhang, L.-L., Ren, J., Huang, X.-L., et al. 2021, ApJ, 917, 95
Zhu, Z. P., Liu, X., Fu, S. Y., et al. 2020a, GRB Coordinates Network, Circular Service, 28653
Zhu, Z. P., Liu, X., Fu, S. Y., et al. 2020b, GRB Coordinates Network, Circular Service, 28677